

The landscape of disk outflows from black hole - neutron star mergers

Rodrigo Fernández¹★, Francois Foucart², Jonas Lippuner^{3,4}

¹*Department of Physics, University of Alberta, Edmonton, AB T6G 2E1, Canada*

²*Department of Physics and Astronomy, University of New Hampshire, Durham, NH 03824, USA*

³*CCS-2, Los Alamos National Laboratory, Los Alamos, NM 87545, USA*

⁴*Center for Theoretical Astrophysics, Los Alamos National Laboratory, Los Alamos, NM 87545, USA*

16 June 2022

ABSTRACT

We investigate mass ejection from accretion disks formed in mergers of black holes (BHs) and neutron stars (NSs). The third observing run of the LIGO/Virgo interferometers provided BH-NS candidate events that yielded no electromagnetic (EM) counterparts. The broad range of disk configurations expected from BH-NS mergers motivates a thorough exploration of parameter space to improve EM signal predictions. Here we conduct 27 high-resolution, axisymmetric, long-term hydrodynamic simulations of the viscous evolution of black hole accretion disks that include neutrino emission/absorption effects and post-processing with a nuclear reaction network. In the absence of magnetic fields, these simulations provide a lower-limit to the fraction of the initial disk mass ejected. We find a nearly linear inverse dependence of this fraction on disk compactness (BH mass over initial disk radius). The dependence is related to the fraction of the disk mass accreted at the time when weak interactions freeze out. We also characterize a trend of decreasing ejected fraction and decreasing lanthanide/actinide content with increasing disk mass at fixed BH mass. This trend results from a longer time to reach weak freezeout and an increasingly dominant role of neutrino absorption at higher disk masses. We provide estimates of the radioactive luminosity from the disk outflow alone available to power kilonovae over the range of BH and NS combinations studied, finding a spread of two orders of magnitude. For most of the BH-NS parameter space, the disk outflow contribution is well below the kilonova mass upper limits for S190814bv.

Key words: accretion, accretion disks – dense matter – gravitational waves – hydrodynamics – neutrinos – nuclear reactions, nucleosynthesis, abundances

1 INTRODUCTION

The Advanced LIGO interferometer has completed three observing runs – with Advanced Virgo joining part of the way – resulting in the official detection of 11 binary black hole (BHs) mergers and two neutron star (NS) mergers (Abbott et al. 2019, 2020; LIGO Scientific Collaboration & Virgo Collaboration 2020), with many more in candidate status at the time of this writing. Only one of these events (GW170817), however, has had electromagnetic (EM) counterparts detected (Abbott et al. 2017). The increased sensitivity of the third observing run resulted in a larger trigger rate and, for the first time, candidates compatible with a BH-NS merger (e.g., LIGO Scientific Collaboration & Virgo Collaboration 2019; Coughlin et al. 2020; Ackley et al. 2020; Andreoni et al. 2020; Vieira et al. 2020). While multiple reasons can account for the lack of an EM detection (such as a large distance, large localization area, galactic extinction, or Sun constraints; e.g. Foley et al. 2020), the possibility remains

that these sources were intrinsically fainter than the kilonova from GW170817.

BH-NS mergers can lead to a wide range of ejected masses depending on whether the NS is tidally disrupted by the BH. The outcome depends on the masses of the ingoing BH and NS, as well as on the spin of the BH and the compactness of the NS (e.g., Foucart et al. 2018). The dynamical ejecta emerges as a very neutron-rich, equatorial tidal tail that quickly leaves the system. The nucleosynthesis properties and contribution to the kilonova transient are mostly set at the time of ejection (e.g., Roberts et al. 2017), and its properties can be parameterized by direct comparison with dynamical merger simulations (e.g., Kawaguchi et al. 2016; Krüger & Foucart 2020).

The accretion disk, on the other hand, ejects mass on a longer timescale, as angular momentum is transported initially by gravitational torques and later by magnetohydrodynamic (MHD) turbulence (see, e.g., Fernández & Metzger 2016; Shibata & Hotokezaka 2019 for reviews). This longer evolutionary timescale allows weak interactions to modify the composition, resulting in a different r -

★ E-mail: rafernan@ualberta.ca

process yield (and possibly a different kilonova color) than the dynamical ejecta. The complexity of this evolution make it very expensive to realistically model the disk, however. Only a handful of three-dimensional general-relativistic (GR) MHD simulations of disks around BHs have been carried out including at least some important microphysics or neutrino effects (Siegel & Metzger 2017; Hossein Nouri et al. 2018; Siegel & Metzger 2018; Fernández et al. 2019; Miller et al. 2019; Christie et al. 2019). Furthermore, all of these simulations either focus on a narrow subset of parameter space and/or do not evolve the system for long enough to achieve completion of mass ejection.

More extensive studies of BH accretion disks have been carried out using axisymmetric hydrodynamic simulations with a wide variety of approximations to the physics (Fernández & Metzger 2013; Just et al. 2015; Fernández et al. 2015a; Fujibayashi et al. 2020). None of these studies covers a significant fraction of all the possible BH accretion disk configurations, however.

Despite missing the magnetic field, hydrodynamic simulations can provide a good description of the late-time thermal component of the outflow that arises when weak interactions freeze out (Metzger et al. 2009) and heating of the disk by viscous stresses (in lieu of MHD turbulence) is unbalanced. Close comparison between GRMHD and hydrodynamic simulations show that the latter provide a lower limit to the fraction of the disk ejected, with magnetic enhancements dependent on the strength of the initial poloidal field in the disk (Fernández et al. 2019; Christie et al. 2019).

Here we carry out an extensive set of long-term hydrodynamic simulations of accretion disks around BH remnants, with the aim of sampling the entirety of the parameter space resulting from BH-NS mergers, and thereby improving parameter estimation models that take disk outflow properties as input (e.g., Barbieri et al. 2019; Hinderer et al. 2019; Coughlin et al. 2020). Along the way, a broad probe of parameter space allows to identify trends in the disk ejection physics, helping to focus on areas where improvements in the physics (e.g. neutrino transport) have the most impact. Finally, by providing a lower limit to the disk mass ejected, we are also estimating the lower limit to the raw radioactive heating available to power kilonova transients.

The structure of the paper is as follows. Section 2 presents our methods, including our choice of initial conditions from the plausible parameter space of BH-NS mergers. Section 3 presents our results, divided into mass ejection, outflow composition, and implications for EM counterparts. We close with a summary and discussion in Section 4.

2 METHODS

2.1 Initial conditions

In order to sample representative initial disk masses for our simulations, we map the parameter space of BH-NS merger remnants using analytical formulae that are calibrated to numerical relativity simulations. For a given ingoing BH mass $M_{\text{bh(in)}}$ and NS mass M_{ns} , we uniformly sample the range 9–13 km for NS radii and 0–0.7 for the ingoing BH spin, and compute distributions of (1) the remnant baryon mass left outside the BH using the formula of Foucart et al. (2018), (2) the disk mass using the formula of Krüger & Foucart (2020) for the dynamical ejecta, and (3) the post-merger BH mass $M_{\text{bh(out)}}$ and its spin using the formulae of Pannarale (2014) and the output from steps (1)-(2). This approach is intended to be agnostic about the properties of the EOS of dense matter and initial BH spin distribution, within plausible limits.

The resulting cumulative distributions of initial disk masses are shown in Figure 1 for two NS masses $\{1.35, 1.45\} M_{\odot}$ and ingoing BH masses such that the median value of $M_{\text{bh(out)}}$ is $\{3, 5, 8, 10, 15\} M_{\odot}$. The lowest post-merger BH mass is chosen to explore the hypothetical case of a very low-mass ingoing BH, or the prompt collapse of a NS-NS system. The highest BH mass is chosen such that at least 10% of mergers result in disruption. Median disk masses range from $0.1 M_{\odot}$ for the $3 M_{\odot}$ post-merger BH, to $0.02 M_{\odot}$ for the $15 M_{\odot}$ BH. In most cases, sensitivity to the specific choice of NS mass does alter the shape of the histogram but not the extreme values. The post-merger BH spin distributions have medians in the range 0.85–0.9, except for the lowest mass BHs considered, which have spins > 0.95 .

For each post-merger BH mass, Figure 1 shows the disk masses sampled in our study. The lowest disk mass in all cases is taken to be $0.01 M_{\odot}$, which is optically thin to neutrinos, while the largest disk mass is such that it is at the uppermost end of plausible values. In all of our models, we take the spin of the post-merger BH to be 0.8, which while somewhat lower than the median values of the distributions obtained, lies within the range of plausible values (except for $M_{\text{bh(out)}} = 3 M_{\odot}$) and does not demand a prohibitively small time step. Furthermore, the effect of BH spin on the disk outflow properties is known, with more mass with higher average electron fraction being ejected for higher BH spins (Fernández et al. 2015a; Fujibayashi et al. 2020).

The remaining initial disk parameters are chosen by inspecting the output of numerical relativity simulations of BH mergers (e.g., Foucart et al. 2019). The radii of maximum disk density are chosen to be $R_{\text{d}} = \{50, 50, 60, 90, 120\}$ km for post-merger BH masses $\{3, 5, 8, 10, 15\} M_{\odot}$, respectively. The entropy of all disks is taken to be $8 k_{\text{B}}$ per baryon, which results in ratios of isothermal sound speed to orbital speed $\sim 10 - 30\%$ at the point of maximum density. While this choice has some effect on the amount of mass ejected, we use a constant value for uniformity. Finally, the default electron fraction of the disks is set to $Y_{e,\text{ini}} = 0.2$, although we vary this parameter in our simulations given that it is dependent on the quality of the neutrino transport implementation in the merger simulation, and has a non-negligible effect on the disk outflow composition.

2.2 Hydrodynamic Simulations

We perform time-dependent hydrodynamic simulations with FLASH version 3.2 (Fryxell et al. 2000; Dubey et al. 2009), with the modifications described in Fernández & Metzger (2013), Metzger & Fernández (2014), Fernández et al. (2015a), and Lippuner et al. (2017). The code solves the Euler equations in axisymmetric spherical polar coordinates (r, θ) , subject to source terms that include the pseudo-Newtonian gravitational potential of a spinning BH (Artemova et al. 1996) without disk self-gravity, shear viscosity with an α parameterization (Shakura & Sunyaev 1973), and a leakage scheme for neutrino emission, with absorption included as a disk-like light bulb (Fernández & Metzger 2013; Metzger & Fernández 2014). We only include electron type neutrinos/antineutrinos interacting with nucleons via charged-current weak interactions. The code employs the equation of state (EOS) of Timmes & Swesty (2000) with the abundances of neutrons, protons, and alpha particles in nuclear statistical equilibrium (NSE) above a temperature $T = 5 \times 10^9$ K and accounting for the nuclear binding energy of these particles. The electron-positron quantities are extended above the high-density limit of the table using analytic expressions (Bludman & van Ripper 1978; Bethe et al. 1980).

The initial condition is an equilibrium torus with constant an-

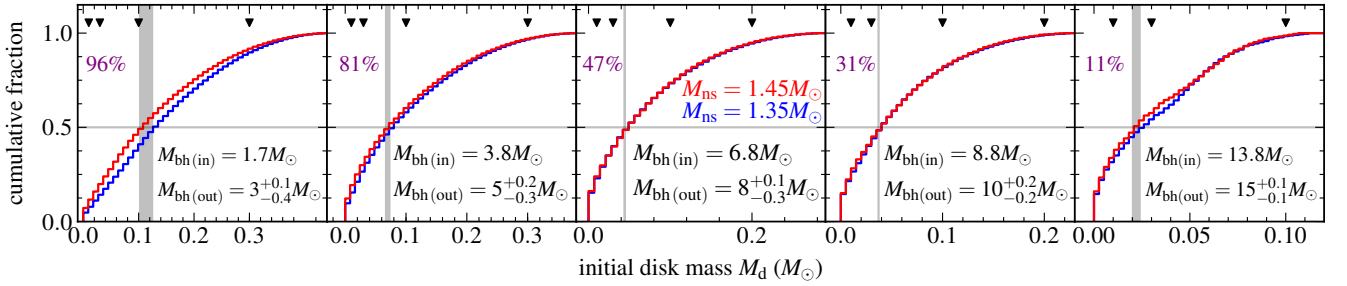


Figure 1. Cumulative distribution of post-merger disk masses, obtained by using analytic formulae for the post-merger BH mass and spin (Pannarale 2014), remnant mass outside the BH (Foucart et al. 2018), and mass in dynamical ejecta (Krüger & Foucart 2020). For fixed ingoing NS mass M_{ns} and BH mass $M_{\text{bh(in)}}$, the intervals 9 – 13 km for NS radii and 0 – 0.7 for ingoing BH spins are uniformly sampled. The uncertainty range in the post-merger BH mass $M_{\text{bh(out)}}$ indicates the range in median values obtained by using the NS masses shown, with the central value corresponding to $M_{\text{ns}} = 1.4M_{\odot}$. The triangles indicate the initial disk masses selected for our hydrodynamic simulations (c.f. Table 1). The fraction of mergers that result in NS disruption for each $\{M_{\text{bh(in)}}, M_{\text{ns}}\}$ pair is shown in purple.

gular momentum, entropy, and electron fraction, with mass fractions assumed to be in NSE (e.g., Fernández & Metzger 2013). Parameters are chosen according to §2.1. The floor of density is set to 10 g cm^{-3} at $r = 4R_{\text{d}}$, and has an initial radial dependence r^{-2} . For $r \leq 4R_{\text{d}}$, the radial exponent of the floor is smoothly brought to zero on a timescale of 40 orbital times at $r = R_{\text{d}}$, reaching a flat floor in this region (Fernández et al. 2019, see also Just et al. 2015). The initial ambient density is set at 1.1 times the floor.

The computational domain extends from an inner radius r_{in} midway between the radius of the innermost stable circular orbit (ISCO) r_{ISCO} and the BH horizon, to an outer radius $r_{\text{out}} = 10^4 r_{\text{in}}$, with the polar angle spanning the range $[0, \pi]$. The grid is discretized logarithmically in radius, using 128 cells per decade, and a polar grid equispaced in $\cos \theta$ using 112 cells. On the equatorial plane, this results in a spacing $\Delta r/r \simeq 1.8\% \simeq 1^\circ \simeq \Delta \theta$. This resolution is double that of the models in Fernández et al. (2017), equivalent to that of the high-resolution models of Fernández & Metzger (2013) and Fernández et al. (2015a), and the same as in Fahlman & Fernández (2018) and the hydrodynamic models of Fernández et al. (2019). The boundary conditions are set to outflow in radius and reflecting in θ .

2.3 Nuclear Reaction Network Post-Processing

Passive tracer particles are initially placed in the disk following the density distribution. For each hydrodynamic simulation we employ 10^4 particles, each representing an equal amount of mass. Particles are advected with the flow and record various kinematic and thermodynamic quantities as a function of time. Particles that are ejected with positive Bernoulli parameter beyond a radius of 10^9 cm by the end of the simulation are considered to be part of the disk outflow.

Outflow trajectories are post-processed with the nuclear reaction network SkyNet (Lippuner & Roberts 2017), using the same settings as in Lippuner et al. (2017). The network employs 7843 nuclides and more than 1.4×10^5 reactions, including strong forward reaction rates from the REACLIB database (Cyburt et al. 2010) with inverse rates computed from detailed balance; spontaneous and neutron-induced fission rates from Frankel & Metropolis (1947), Mamdouh et al. (2001), Wahl (2002), and Panov et al. (2010); weak rates from Fuller et al. (1982), Oda et al. (1994), Langanke & Martínez-Pinedo (2000), and the REACLIB database;

and nuclear masses from the REACLIB database, which includes experimental values were available, or otherwise theoretical masses from the finite-range droplet macroscopic model (FRDM) of Möller et al. (2016).

The rates of electron neutrino/antineutrino absorption/emission recorded by the trajectory are included in the evolution of the proton and neutron fraction. Likewise, the temperature and entropy are evolved self-consistently by accounting for nuclear heating from the network, as well as viscous heating and neutrino heating/cooling in the hydrodynamic simulation as recorded by the trajectory.

Processing begins when the trajectory reaches 10 GK for the last time, or when the temperature is maximal if lower than 10 GK at all times. For the portion of the evolution in which the temperature is higher than 7 GK, abundances are evolved in NSE, subject to neutrino interactions, while full network integration is carried out at lower temperatures. Trajectories are extended beyond the end of the simulation (12 – 25 s) by assuming that the density decays with time as t^{-3} , to allow r -process nuclei with long half-lives to decay. Since the r -process is complete by the time this transition is made, most of the nuclear heating has already been deposited and the exact time dependence of the density decay is not important. While trajectories are evolved until 30 yr, information is extracted at $t = 1 \text{ day}$ and $t = 1 \text{ week}$ to estimate the properties of the kilonova at peak.

2.4 Models Evolved

Table 1 shows all of the hydrodynamic models we evolve. As a baseline set, we take disks with initial conditions as described in §2.1: black hole and disk masses as in Figure 1, initial entropy $8k_{\text{B}}$ per baryon, and initial electron fraction $Y_{\text{e,ini}} = 0.2$. Model names follow the convention bXXdYY, where XX and YY refer to the BH mass and disk mass, respectively. Tori are constructed as an equilibrium solution to the momentum equation with constant Bernoulli parameter, constant angular momentum, and the pseudo-Newtonian potential of the BH (Fernández & Metzger 2013). The torus shape is controlled by a dimensionless distortion parameter d (Stone et al. 1999) which is solved for by fixing the entropy, Y_{e} , and torus mass. The distortion parameter is related to the torus initial Bernoulli parameter b_{ini} , black hole mass $M_{\text{bh}} \equiv M_{\text{bh(out)}}$,

Table 1. Hydrodynamic models evolved and input parameters. Columns from left to right show model name, black hole mass, disk mass, radius of initial disk density peak, initial electron fraction, torus distortion parameter, viscosity parameter, and maximum evolution time.

Model	M_{bh} (M_{\odot})	M_{d} (M_{\odot})	R_{d} (km)	$Y_{e,\text{ini}}$	d	α	t_{max} (s)
b03d01	3	0.01	50	0.20	1.52	0.03	16.5
b03d03		0.03			1.82		
b03d10		0.10			2.40		
b03d30		0.30			3.37		
b05d01	5	0.01			1.39		12.2
b05d03		0.03			1.59		
b05d10		0.10			1.97		
b05d30		0.30			2.57		
b08d01	8	0.01	60		1.30		12.1
b08d03		0.03			1.43		
b08d10		0.10			1.67		
b08d20		0.20			1.87		
b10d01	10	0.01	90		1.20		20.6
b10d03		0.03			1.30		
b10d10		0.10			1.46		
b10d20		0.20			1.59		
b15d01	15	0.01	120		1.15		25.4
b15d03		0.03			1.22		
b15d10		0.10			1.32		
b03d01-y10	3	0.01	50	0.10	1.50		16.5
b03d30-y10		0.30			3.30		
b08d03-y10	8	0.03	60		1.42		12.1
b03d01-y15	3	0.01	50	0.15	1.51		16.5
b03d30-y15		0.30			3.32		
b08d03-y15	8	0.03	60		1.43		12.1
b03d01-v10	3	0.01	50	0.20	1.52	0.10	16.5
b08d03-v10	8	0.03	60		1.43		12.1

and radius of initial density peak R_{d} by

$$b_{\text{ini}} = -\frac{1}{2d} \frac{GM_{\text{bh}}}{R_{\text{d}}}. \quad (1)$$

The baseline set is evolved with a viscosity parameter $\alpha = 0.03$

To assess the effects of initial composition, we evolve a few models with lower initial electron fraction than the baseline set $Y_{e,\text{ini}} = \{0.10, 0.15\}$. Likewise, we evolve two models with higher viscosity parameter, $\alpha = 0.1$.

All hydrodynamic models are evolved for 5,000 orbits at the initial density peak radius, which corresponds to $\approx 12 - 25$ s of physical time (Table 1). This time is chosen such that the mass ejection from the disk is mostly complete. Tracer particles from each simulation are then post-processed with the nuclear reaction network as described in §2.3

3 RESULTS

The overall evolution of neutrino cooled accretion disks follows well-known stages (e.g., Popham et al. 1999; Di Matteo et al. 2002; Chen & Beloborodov 2007; Lee et al. 2009). Depending on the initial disk mass, neutrinos can be trapped or escape freely. In the former case, an initial optically thick phase ensues until the density has decreased sufficiently for transparency. Thereafter, neutrino cooling is important compared to viscous heating, the inner disk is

not too thick vertically, and accretion proceeds efficiently. After about a viscous time $R_{\text{d}}^2/(\alpha c_i^2/\Omega_{\text{K}}) \sim \text{few } 100 \text{ ms}$ (with c_i the isothermal sound speed and Ω_{K} the orbital frequency; Shakura & Sunyaev 1973), the density becomes low enough that weak interactions freeze out, shutting down cooling (e.g., Metzger et al. 2009). At this point, the disk is radiatively inefficient, with viscous heating and nuclear recombination of α particles being unbalanced, thus an outflow is launched until no more mass is available to be ejected.

In the absence of magnetic fields, this thermal outflow is the only relevant mass ejection channel when a BH sits at the center, as neutrino-driven winds are weak given that self-irradiation is not efficient (e.g., Just et al. 2015). A comparison with long-term GRMHD simulations shows that the outflow from hydrodynamic simulations is of similar quantity and has similar velocities as the analog process occurring due to dissipation of MHD turbulence (Fernández et al. 2019). The magnetic field provides for additional, faster components that can eject a comparable amount of mass than the thermal outflow.

In the following, we discuss mass ejection properties across the range of models we evolve, the composition of these outflows, and the implications for EM counterparts of BH-NS mergers.

3.1 Mass ejection

The disk mass ejection rate in all directions \dot{M}_{out} is measured at a radius $r_{\text{out}} = 10^9$ cm, far enough outside the disk that mostly complete ejection is achieved before the disk viscously spreads to that radius. Material is considered to be unbound when its Bernoulli parameter

$$b = \frac{1}{2} \left[v_r^2 + v_{\theta}^2 + \left(\frac{j}{r \sin \theta} \right)^2 \right] + e_{\text{int}} + \frac{p}{\rho} + \Phi \quad (2)$$

is positive. In equation (2), v_r and v_{θ} are the radial and meridional velocities, e_{int} is the specific internal energy, p is the pressure, ρ is the density, j is the specific angular momentum, and Φ is the gravitational potential. Table 2 shows the ejected outflow mass M_{ej} – the time integral of \dot{M}_{out} over the simulation – for all models.

The fraction of the initial disk mass ejected is shown in Figure 2 for the baseline model sequence. This fraction ranges from 4% for the heaviest disk with $M_{\text{bh}} = 8M_{\odot}$ to 21% for the lightest disk around the $M_{\text{bh}} = 3M_{\odot}$ BH. The most important trend in mass ejection apparent from Table 2 is a monotonically decreasing ejected fraction with strength of gravity at the disk, $\propto M_{\text{bh}}/R_{\text{d}}$. For convenience, we define a disk compactness parameter as

$$C_{\text{d}} = \left(\frac{M_{\text{bh}}}{5M_{\odot}} \right) \left(\frac{50 \text{ km}}{R_{\text{d}}} \right). \quad (3)$$

Figure 2 also shows that the dependence of the ejected fraction with compactness is approximately linear, although at low BH masses the disk mass becomes an additional factor. This dependence on the strength of gravity has previously been documented in Fernández & Metzger (2013), and is also apparent from the results of Just et al. (2015), Fernández et al. (2017), and Fujibayashi et al. (2020), although this is the first time that it is sampled over an extended region of parameter space.

The second mass ejection trend in all models of the baseline sequence is a monotonic decrease in the ejected fraction with increasing disk mass. Figure 2 shows that the strength of this dependence on disk mass is itself a function of disk compactness, with low-compactness disks being the most sensitive to the initial disk mass, while in high compactness systems this property has a smaller impact on the ejected fraction.

Table 2. Summary of results. Columns from left to right show model name, disk compactness (eq. 3), ejected mass, fraction of initial disk mass ejected $M_{\text{ej}}/M_{\text{d}}$, average outflow velocity, average outflow electron fraction, ejecta mass with $X_{\text{La+Ac}} < 10^{-4}$ (M_{blue}), ejecta mass with $X_{\text{La+Ac}} > \{10^{-4}, 10^{-3}, 10^{-2}\}$ (M_{-4}, M_{-3}, M_{-2}), respectively), and radioactive heating power (in units of 10^{40} erg s^{-1}) at 1 day and 7 days, ignoring thermalization efficiency.

Model	C_{d}	M_{ej} ($10^{-2} M_{\odot}$)	$M_{\text{ej}}/M_{\text{d}}$	$\langle v/c \rangle$ (10^{-2})	$\langle Y_e \rangle$	$M_{\text{blue}}/M_{\text{ej}}$	M_{-4}/M_{ej}	M_{-3}/M_{ej}	M_{-2}/M_{ej}	$L_{40, 1\text{d}}$	$L_{40, 1\text{w}}$
b03d01	0.60	0.21	0.21	3.4	0.28	0.75	0.25	0.18	0.10	8.9	0.99
b03d03		0.57	0.19	3.3	0.28	0.84	0.16	0.09	0.03	21	2.2
b03d10		1.8	0.18	3.4	0.29	0.93	0.07	0.03	0.01	60	5.9
b03d30		4.8	0.16	3.1	0.29	0.86	0.14	0.08	0.05	150	17
b05d01	1.00	0.11	0.11	3.4	0.29	0.72	0.28	0.20	0.09	4.5	0.51
b05d03		0.32	0.11	3.4	0.30	0.87	0.13	0.04	0.02	12	1.2
b05d10		0.98	0.09	3.5	0.31	0.98	0.02	0.01	0.01	30	2.8
b05d30		2.7	0.09	3.1	0.31	0.98	0.02	0.02	0.01	72	6.3
b08d01	1.33	0.05	0.05	3.3	0.28	0.66	0.34	0.25	0.12	2.3	0.25
b08d03		0.15	0.05	3.9	0.30	0.82	0.18	0.08	0.05	5.5	0.58
b08d10		0.49	0.05	3.6	0.33	0.99	0.01	0.01	0.00	13	1.1
b08d20		0.87	0.04	3.9	0.33	1.00	0.00	0.00	0.00	19	1.6
b10d01	1.11	0.09	0.09	3.4	0.29	0.72	0.28	0.20	0.12	3.9	0.47
b10d03		0.27	0.09	3.4	0.31	0.86	0.14	0.06	0.02	8.6	0.99
b10d10		0.90	0.09	3.3	0.33	0.98	0.02	0.02	0.01	23	2.5
b10d20		1.7	0.08	3.5	0.34	0.99	0.01	0.01	0.00	40	4.3
b15d01	1.25	0.06	0.06	3.7	0.27	0.63	0.37	0.27	0.14	2.9	0.35
b15d03		0.19	0.06	3.5	0.30	0.79	0.21	0.12	0.04	6.8	0.80
b15d10		0.62	0.06	3.5	0.34	0.98	0.02	0.01	0.01	16	1.6
b03d01-y10	0.60	0.21	0.21	3.4	0.26	0.62	0.38	0.32	0.25	9.0	1.1
b03d30-y10		4.1	0.14	3.4	0.28	0.86	0.14	0.10	0.08	130	13
b08d03-y10	1.33	0.16	0.05	3.7	0.29	0.75	0.25	0.20	0.16	6.0	0.71
b03d01-y15	0.60	0.20	0.20	3.3	0.27	0.69	0.31	0.25	0.19	8.9	1.1
b03d30-y15		4.3	0.14	2.8	0.28	0.85	0.15	0.12	0.09	120	13
b08d03-y15	1.33	0.15	0.05	3.7	0.30	0.76	0.24	0.18	0.10	5.5	0.64
b03d03-v10	0.60	0.28	0.28	5.6	0.27	0.55	0.45	0.41	0.34	13	1.2
b08d03-v10	1.33	0.31	0.10	5.5	0.31	0.77	0.23	0.20	0.15	12	0.83

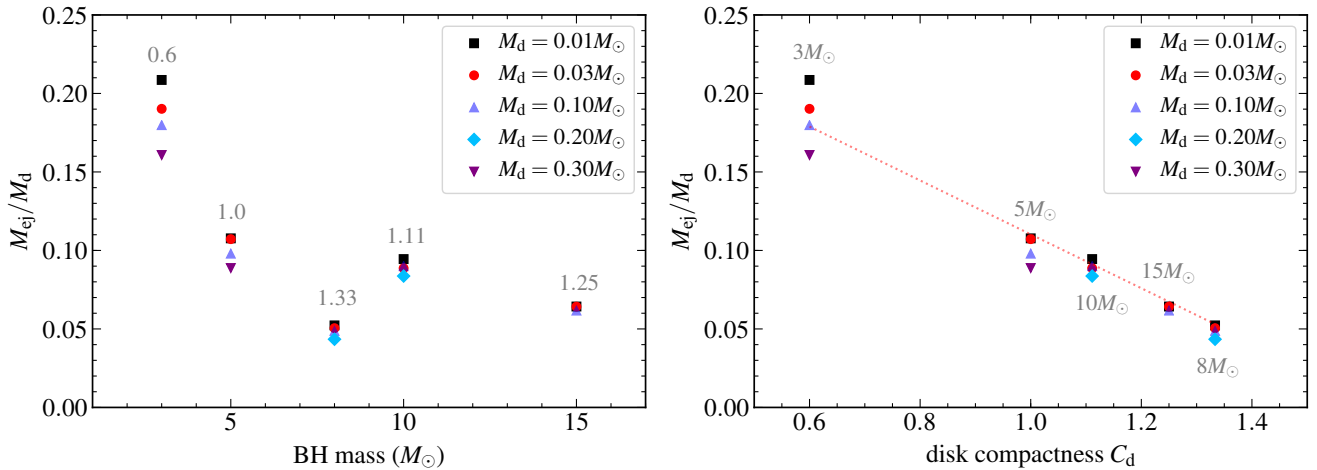


Figure 2. *Left:* Fraction of the initial disk mass ejected with positive Bernoulli parameter (eq. 2) as a function of BH mass. Different symbols and colors correspond to different disk masses, as labeled. The gray number above each symbol column corresponds to the disk compactness parameter C_{d} (eq. 3). *Right:* Fraction of the initial disk mass ejected as a function of disk compactness parameter, using the same color and symbol coding as in the left panel. The gray numbers above each symbol column denote the corresponding BH mass. The red dotted line is a linear fit to the ejected fraction for disks with $M_{\text{d}} = 0.03 M_{\odot}$. GRMHD effects can enhance the ejected fraction and average velocity by up to a factor of ~ 2 relative to hydrodynamic models (Fernández et al. 2019).

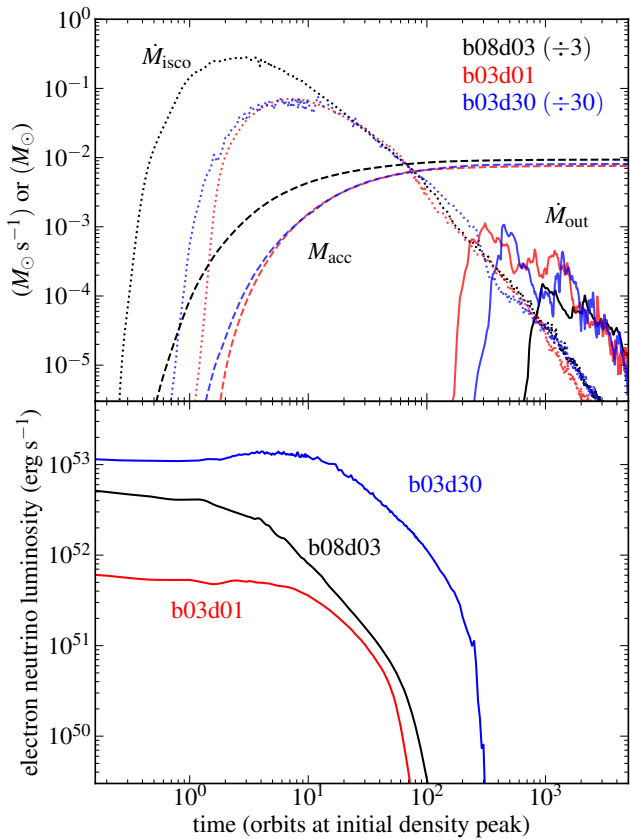


Figure 3. *Top:* Mass accretion rate at the ISCO (\dot{M}_{ISCO} , dotted lines), cumulative accreted mass at the ISCO (M_{acc} , dashes lines), and mass outflow rate in unbound material at $r = 10^9$ cm (\dot{M}_{out} , solid lines) as a function of time for models b08d03 (high-compactness), b03d01 (low compactness, low disk mass), and b03d30 (low compactness, high disk mass), as labeled. To facilitate comparison, the data from models b08d03 and b03d30 has been normalized to a disk mass of $0.01 M_{\odot}$ (as in model b03d01). *Bottom:* Electron neutrino luminosity for models b08d03, b03d01, and b03d30, as labeled. The fraction of the disk ejected is related to the fraction of the disk accreted at the time when weak interactions freeze out.

The physical origin of these trends in mass ejection can be traced back to the nature of the ejection mechanism. Most of the outflow is launched once weak interactions freeze out in the disk, removing the source of cooling. The fraction of the disk mass available to be ejected depends on how much has already been lost to accretion onto the BH by the time freezeout occurs. This interplay is illustrated in Figure 3, which shows the evolution of the mass accretion rate (\dot{M}_{ISCO}) and cumulative mass accreted at the ISCO (M_{acc}), mass ejection rate at large radii (\dot{M}_{out}), and the electron neutrino luminosity.

In the model with the highest compactness (b08d03), accretion starts much earlier when measured in orbital times than in the lower-compactness models. By the time weak interactions freeze out (steep plummet in neutrino luminosity at about 100 orbits) a significant fraction of the disk (85%) has already been accreted to the BH. This earlier onset of accretion, despite having the same viscosity parameter, is due to the disk being closer to the ISCO. In terms of dimensionless numbers: $r_{\text{ISCO}}/R_{\text{d}} = \{0.26, 0.57\}$ for $C_{\text{d}} = \{0.60, 1.33\}$, respectively.

For disks of the same compactness, the evolution of the accretion rate is very similar. Figure 3 shows that mass ejection begins

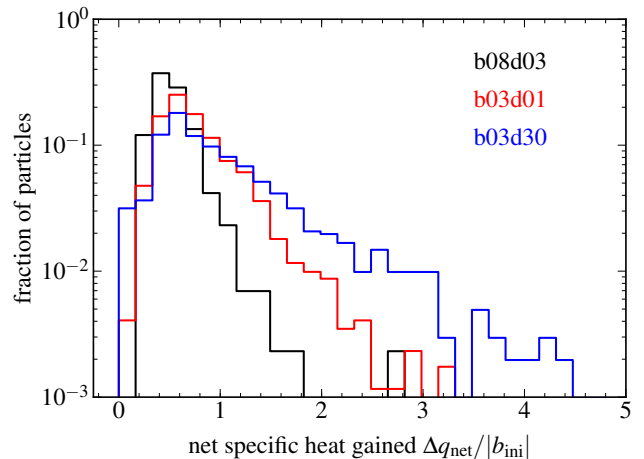


Figure 4. Distribution of net specific heat gained by tracer particles due to source terms (eq. 7) in the hydrodynamic evolution of models b08d03, b03d01, and b03d30, as labeled. The heat gain is normalized to the initial Bernoulli parameter in the disk (eq. 1).

later in the more massive disk, which also takes longer time to reach freezeout of weak interactions. More massive disks are more optically thick to neutrinos owing to their higher initial density, and for the same strength of viscosity, it takes more orbits for the density to decrease to a level where neutrino processes are no longer effective in cooling the disk. At the time when the neutrino luminosity reaches $10^{50} \text{ erg s}^{-1}$, models b03d01 and b03d30 have accreted 60% and 78% of their initial disk masses, respectively.

The density dependence of the neutrino optical depth is not the only factor influencing the freezeout time. Table 1 and equation (1) show that to keep the entropy constant, initial equilibrium disks with higher masses also have a higher internal energy content and therefore higher temperatures. This effect is stronger for lower compactness configurations. While disk material is more weakly bound, it can also radiate neutrinos at relevant levels for a longer time, and so this acts in the direction of delaying the onset of mass ejection. The post-merger entropy of the disk thus is an important parameter to keep track of in dynamical merger simulations given its effect on mass ejection efficiency.

Using the outflow trajectories from hydrodynamic simulations we can further analyze the energetics of mass ejection. In particular, we can quantify the strength and importance of different processes that change the heat content of the fluid: viscous heating, neutrino heating/cooling, and nuclear recombination of alpha particles. For each trajectory, we compute the time integral of the local energy source term, yielding the heat gained or lost by the fluid element per unit mass:

$$\Delta q_{\text{visc}} = \int_0^{t_{\text{max,p}}} \dot{q}_{\text{visc}} dt \quad (4)$$

$$\Delta q_{\nu} = \int_0^{t_{\text{max,p}}} \dot{q}_{\nu} dt \quad (5)$$

$$\Delta q_{\alpha} = \frac{B_{\alpha}}{m_{\alpha}} [X_{\alpha}(t_{\text{max,p}}) - X_{\alpha}(0)] \quad (6)$$

$$\Delta q_{\text{net}} = \Delta q_{\text{visc}} + \Delta q_{\nu} + \Delta q_{\alpha}, \quad (7)$$

where $\{\dot{q}_{\text{visc}}, \dot{q}_{\nu}\}$ stand for viscous heating and neutrino heating/cooling, respectively, $B_{\alpha}/m_{\alpha} \approx 6.8 \times 10^{18} \text{ erg g}^{-1}$ is the specific nuclear binding energy of alpha particles, X_{α} is the mass fraction of

Table 3. Average time-integrated heat gain or loss per unit mass (eqns. 4-7), and change in Y_e (eqns. 10-17), due to various processes acting on tracer particles during the hydrodynamic evolution of selected models. The specific heat gain due to process i is normalized as $\bar{\Delta}q_{i,19} = \bar{\Delta}q_i / (10^{19} \text{ erg g}^{-1})$, and $\bar{\Delta}$ denotes average over all outflow particles. Each quantity is separately rounded for clarity, net sums match when including all significant digits.

Model	$\bar{\Delta}q_{\text{net}}/ b_{\text{ini}} $	$\bar{\Delta}q_{\text{net},19}$	$\bar{\Delta}q_{\text{visc},19}$	$\bar{\Delta}q_{\nu,19}$	$\bar{\Delta}q_{\alpha,19}$	$\bar{\Delta}Y_e^{\text{net}}$	$\bar{\Delta}Y_e^{\text{em},\nu e}$	$\bar{\Delta}Y_e^{\text{em},\bar{\nu}e}$	$\bar{\Delta}Y_e^{\text{abs},\nu e}$	$\bar{\Delta}Y_e^{\text{abs},\bar{\nu}e}$	$\bar{\Delta}Y_e^{\text{em}}$	$\bar{\Delta}Y_e^{\text{abs}}$
b03d01	0.81	2.1	2.6	-0.8	0.3	0.08	0.42	0.45	0.07	0.01	0.03	0.05
b03d03	0.79	1.7	2.5	-1.1	0.3	0.08	0.64	0.61	0.15	0.04	-0.03	0.12
b03d10	0.91	1.5	2.8	-1.6	0.3	0.09	1.00	0.91	0.25	0.07	-0.09	0.18
b03d30	1.12	1.3	2.9	-1.9	0.3	0.09	1.12	1.04	0.26	0.08	-0.08	0.18
b08d01	0.51	3.5	3.9	-0.7	0.3	0.09	0.34	0.41	0.03	0.01	0.07	0.02
b08d03	0.55	3.4	4.2	-1.1	0.4	0.10	0.53	0.58	0.07	0.02	0.05	0.05
b08d10	0.60	3.2	4.5	-1.7	0.4	0.11	0.81	0.83	0.13	0.04	0.02	0.09
b08d20	0.66	3.1	4.9	-2.2	0.4	0.13	1.10	1.08	0.21	0.06	-0.02	0.15
b03d01-y10	0.79	2.1	2.6	-0.8	0.3	0.16	0.37	0.48	0.07	0.01	0.11	0.05
b03d01-y15	0.78	2.1	2.6	-0.8	0.3	0.12	0.40	0.47	0.07	0.01	0.07	0.05
b03d01-v10	0.94	2.5	2.7	-0.5	0.3	0.07	0.22	0.25	0.05	0.02	0.04	0.03
b03d30-y10	1.16	1.4	3.1	-2.1	0.3	0.19	1.16	1.16	0.27	0.08	0.00	0.19
b03d30-y15	1.05	1.3	2.7	-1.8	0.3	0.13	1.05	1.01	0.25	0.07	-0.04	0.17
b08d03-y10	0.53	3.3	4.0	-1.1	0.3	0.19	0.46	0.60	0.07	0.02	0.14	0.05
b08d03-y15	0.55	3.4	4.3	-1.2	0.3	0.15	0.55	0.65	0.07	0.02	0.10	0.05
b08d03-v10	0.67	4.2	4.9	-1.0	0.4	0.12	0.40	0.48	0.06	0.02	0.08	0.04

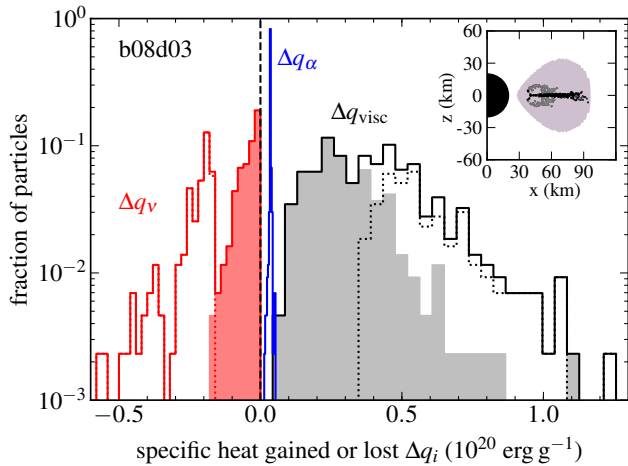


Figure 5. Distribution of specific heat gained or lost by tracer particles due to source terms (eqns. 4-6), as labeled, in the hydrodynamic evolution of model b08d03. The inset shows a snapshot of the initial positions of outflow particles in the disk, with gray/black particles corresponding to the shaded/dotted subsets of the neutrino and viscous heat gain histograms, respectively (see also Wu et al. 2016 for a larger plot of the initial particle distribution).

alpha particles, $t_{\text{max,p}}$ is the maximum time for the particle evolution, either when it leaves the outer boundary of the computational domain or when the simulation ends, whichever is shorter, and Δq_i is the heat gained or lost from process i . The resulting quantities are shown in Table 3 for selected models.

Figure 4 shows the distribution of net heat gained Δq_{net} (eq. 7) by outflow particles for the same set of simulations shown in Figure 3. Specific energies are shown in units of the initial Bernoulli parameter of the disk (equation 1). In all three models, the distribution shows a peak at around 60% of $|b_{\text{ini}}|$, with a tail toward high gain that is more extended for less compact models and higher disk masses. For a large fraction of the outflow, unbinding is not

completely achieved by absorption of heat alone, which means that a significant part of the energy gain comes from adiabatic work. Disks with higher compactness are also less effective at absorbing heat, despite the fact that the absolute value of the net heat gain is higher (Table 3).

For individual models, viscous heating and nuclear recombination contribute with net heating, while neutrinos primarily cool the disk (Table 3). This is illustrated in Figure 5, which shows the distribution of the individual heating/cooling terms for the outflow from model b08d03. While there is a non-negligible fraction of particles for which neutrinos provide net heating, the magnitude of this heating ($\sim 10^{17} \text{ erg g}^{-1}$) is dynamically negligible when compared to the dominant source terms ($\sim 10^{19} \text{ erg g}^{-1}$).

The integrated heat gain due to α particle recombination in the hydrodynamic simulation is sub-dominant compared to that from viscous heating. Despite its low global value, however, the heating due to α recombination is deposited over a short amount of time as the outflow is launched, and it can become comparable or even exceed the rate of viscous heating in this phase. The bulk of neutrino heating and cooling takes place before weak freezeout. Figure 5 shows that the nuclear recombination gain is narrowly distributed around the mean value, $3 - 4 \times 10^{18} \text{ erg g}^{-1}$ (Table 3). This value can be understood from the fact that upon expansion and cooling, all fluid elements achieve the maximal alpha particle mass fraction set by charge conservation, $X_{\alpha,\text{max}} = 2Y_e$. The average electron fraction of the outflow $\langle Y_e \rangle \approx 0.3$ (Table 2), then sets the average amount of energy gained.

Figure 5 also shows that the tracer particles in model b08d03 follow bimodal distributions of viscous heating and neutrino cooling. This bimodality can be traced back to the initial positions of the particles in the disk. These particles originate from two regions: (1) the equatorial plane of the disk, and (2) regions above the equatorial plane around the initial density peak (see also Wu et al. 2016). The first group of particles experiences stronger viscous heating and neutrino cooling, while the second group experiences heating or cooling with less intensity. The latter group includes all the particles that experience net neutrino heating. The initial position of the particles is related to the way the disk overturns in the poloidal

direction due to viscous heating, and may differ from that obtained when MHD turbulence transports angular momentum.

The fraction of the disk mass ejected and average outflow velocity are nearly insensitive to the initial Y_e of the disk except for very massive disks in low-compactness systems, where differences of a few percent of the disk mass can arise (Table 3). Changes in the viscosity parameter, on the other hand, result in important changes to both ejected fraction and outflow velocity. The average outflow radial velocity is in the range 0.03 – 0.04 c for all models that use $\alpha = 0.03$, while this average increases to 0.05–0.06 c for the models with $\alpha = 0.1$. The fraction of the disk mass ejected increases by $\sim 30\%$ for the model with low compactness (b03d01-v10) and by a factor of 2 for the high compactness model (b08d03-v10). Table 3 shows that the increase in the viscosity parameter results in more viscous heating in the high-compactness model b08d03-v10 and less neutrino cooling in the least compact model b03d01-v10, in both cases increasing the net heat gain of the outflow.

3.2 Outflow Composition

Table 2 shows that the average electron fraction of the disk outflow is in the range 0.25 – 0.35 for all simulated models. These values are just above the critical transition at which the nucleosynthesis changes from rich to poor in elements with mass numbers $A > 130$ (e.g., Kasen et al. 2015; Lippuner & Roberts 2015). For the purposes of predicting kilonova properties, the mass fraction in lanthanides ($57 \leq Z \leq 72$, with Z the atomic number) and actinides ($89 \leq Z \leq 104$) is the most important, since these species have an outside influence on the ejecta opacity – and therefore on the kilonova color, luminosity, and duration – given their atomic complexity (Tanaka & Hotokezaka 2013; Kasen et al. 2013; Barnes & Kasen 2013; Fontes et al. 2015; Tanaka et al. 2019).

We therefore refine our diagnostic of the outflow composition by analyzing the output of post-processed tracer particles with SkyNet (§2.3). For each simulation, we report in Table 2 the fraction of the outflow particles with lanthanide and actinide mass fraction $X_{\text{La}} + X_{\text{Ac}} < 10^{-4}$ and define it as the ‘blue mass’

$$M_{\text{blue}} = \int_0^{10^{-4}} \frac{dM_{\text{ej}}}{d(X_{\text{La}} + X_{\text{Ac}})} d(X_{\text{La}} + X_{\text{Ac}}). \quad (8)$$

The value of 10^{-4} is small enough that the outflow opacity is indistinguishable from that dominated by iron-group elements (Kasen et al. 2013). Likewise, we define three ‘red’ masses

$$M_{-k} = \int_{10^{-k}}^1 \frac{dM_{\text{ej}}}{d(X_{\text{La}} + X_{\text{Ac}})} d(X_{\text{La}} + X_{\text{Ac}}). \quad (9)$$

using $-k = \{-4, -3, -2\}$. These four numbers provide a description of the incidence of heavy r -process elements in the ejecta that, while coarser than detailed abundances, is more informative than just the electron fraction. Figure 6 shows the distribution of mass fractions at 1 day in the outflow particles from models b08d01–b08d20 (highest compactness), along with the regions encompassed by M_{blue} and M_{-k} , and the isotopic abundances for comparison. At 1 day, the mass fractions of actinides are in general 10 times smaller than that of lanthanides in our models, and thus we lump them together when discussing composition effects (for more detailed studies on actinide production see Eichler et al. 2019 or Holmbeck et al. 2019).

The most robust composition trends from Table 2 are that (1) the majority of the disk outflow mass is lanthanide poor (M_{blue}), and that (2) the fraction of lanthanide poor material is a monotonically increasing function of the disk mass, for constant BH mass.

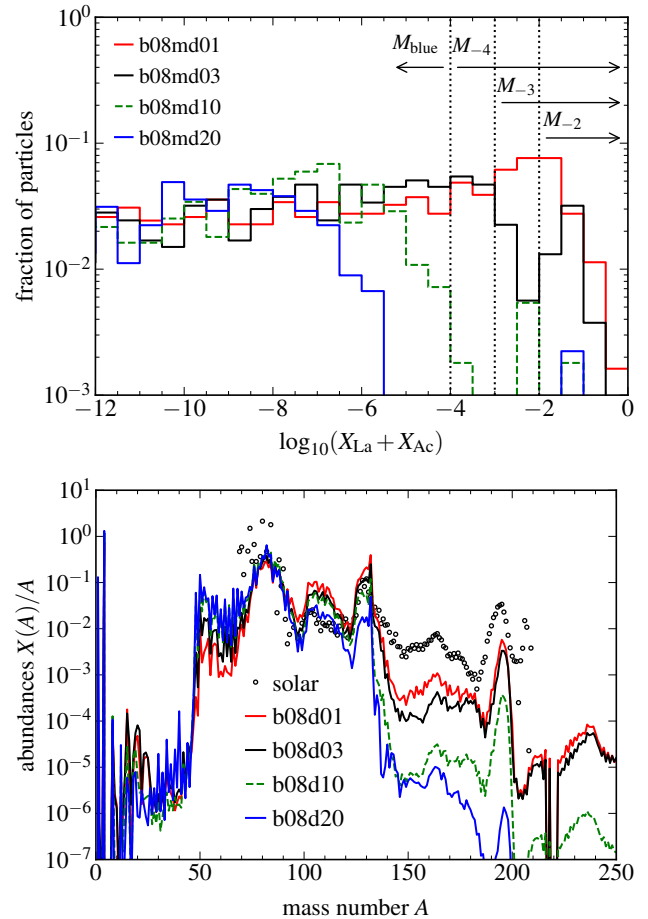


Figure 6. *Top:* Distribution of lanthanide and actinide mass fractions at 1 day, for nuclear-network-processed particles from models b08d01–b08d20, as labeled. Since each particle represents an equal mass element in the disk, a sum over the bins yields the fraction of the mass with a given Lanthanide and Actinide fraction (M_{blue} and $\{M_{-4}, M_{-3}, M_{-2}\}$, c.f. eqns. (8)–(9) and Table 2). The histograms continue to mass fractions lower than 10^{-12} with similar slope, and were truncated for clarity. *Bottom:* Isotopic abundances at 1 day for nuclear-network-processed particles from models b08d01–b08d20, as labeled. Abundances are normalized such that their mass fractions add up to unity. The solar system r -process abundances from Goriely (1999) are normalized to model b08d03 at $A = 130$. Note that the dynamical ejecta is rich in elements with $A > 130$, and in combination with the disk outflow can supply the entire range of r -process elements (e.g., Just et al. 2015).

The dependence on disk mass is clearly illustrated in Figure 6: the fraction of particles with high lanthanide abundance is a steep function of the disk mass, as is the abundance of elements with $A > 130$ (this dependence has also been reported by Just et al. 2015 and Fujibayashi et al. 2020). While there is some dependence on the compactness C_d at constant disk mass, this dependence is not fully monotonic, and is weaker than the dependence on disk mass at fixed compactness. Therefore, this variation with compactness is more likely to be dependent on the details of how the disk evolution is modeled.

The trend of more lanthanide poor ejecta with increasing disk mass is apparent from the distribution of electron fraction (Figure 7). Despite having a very similar average value, the Y_e distribution of model b08d20 extends to significantly higher values than in model b08d01. Naively, one would expect that higher electron fraction

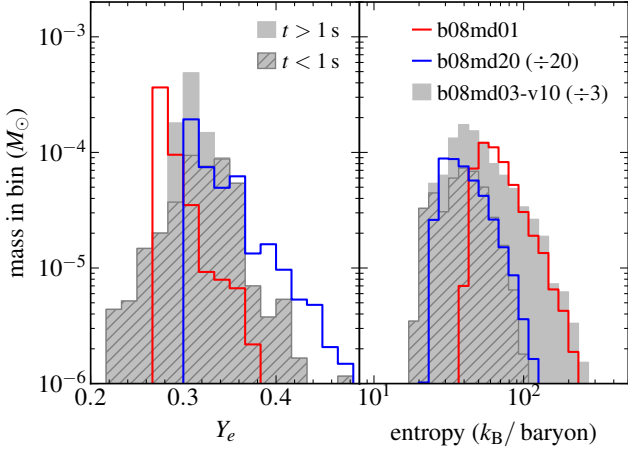


Figure 7. Mass histograms of electron fraction (left) and entropy (right) for models b08d01 (low disk mass), b08d20 (high disk mass), and b08d03-v10 (high viscosity), obtained by the end of the hydrodynamic simulation at $r = 10^9$ cm. To facilitate comparison, histogram masses have been normalized to that of model b08d01. The hatched region is the subset of the histogram of model b08d03-v10 for times $t < 1$ s.

is associated with a higher equilibrium Y_e arising from a higher abundance of positrons given higher entropies (e.g., Beloborodov 2003). However, the entropy distributions of models b08d01 and b08d20 show that the average entropy *decreases* with higher disk masses. The lower entropy can be understood from the fact that the temperature is primarily set by the strength of the gravitational potential once accretion is established, and is similar in both models. On the other hand, the densities are higher at any given time for a higher disk mass, with a correspondingly lower entropy than at lower disk masses.

We can further analyze the evolution of the electron fraction distribution of the outflow by computing the time-integrated contribution of the different neutrino processes that change Y_e . The net rate of change of Y_e due to neutrino emission and absorption arises from the following reactions:

$$\Gamma^{\text{em}, \nu_e} : e^- + p \rightarrow n + \nu_e \quad (10)$$

$$\Gamma^{\text{em}, \bar{\nu}_e} : e^+ + n \rightarrow p + \bar{\nu}_e \quad (11)$$

$$\Gamma^{\text{abs}, \nu_e} : \nu_e + n \rightarrow e^- + p \quad (12)$$

$$\Gamma^{\text{abs}, \bar{\nu}_e} : \bar{\nu}_e + p \rightarrow e^+ + n \quad (13)$$

$$\Gamma^{\text{em}} = \Gamma^{\text{em}, \bar{\nu}_e} - \Gamma^{\text{em}, \nu_e} \quad (14)$$

$$\Gamma^{\text{abs}} = \Gamma^{\text{abs}, \nu_e} - \Gamma^{\text{abs}, \bar{\nu}_e} \quad (15)$$

$$\Gamma^{\text{net}} = \Gamma^{\text{em}} + \Gamma^{\text{abs}} \quad (16)$$

with the net rate setting the overall evolution of the electron fraction in the hydrodynamic simulation: $\partial Y_e / \partial t + \mathbf{v} \cdot \nabla Y_e = \Gamma^{\text{net}}$. For each tracer particle, we compute a separate time integral for each of the rates above, obtaining a contribution to the change in electron fraction:

$$\Delta Y_e^i = \int_0^{t_{\text{max},p}} \Gamma^i dt, \quad (17)$$

where again $t_{\text{max},p}$ is the maximum time of the particle in the simulation.

Table 3 shows that the rates of neutrino emission dominate over neutrino absorption for all models, in line with the overall dominance of neutrino cooling over neutrino heating (c.f. Figure 5).

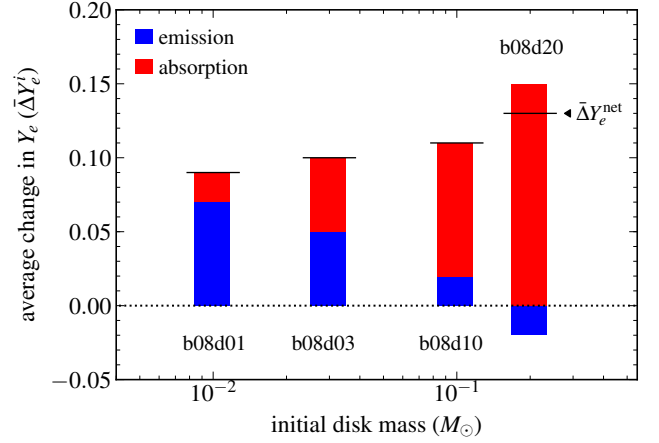


Figure 8. Average electron fraction change in particles due to neutrino emission or absorption (eqns. 10-16 and 17, Table 3), during the hydrodynamic evolution of models b08d01-b08d20, as labeled. The black horizontal lines denote the net change in Y_e when including all processes. The relative importance of neutrino absorption increases as the disk mass increases, all else being equal, accounting for the higher Y_e of the outflow with lower overall entropies (Figure 7).

However, the change in Y_e is set by *differences* in the rates of neutrino/antineutrino emission and absorption. If the two emission rates are closer in magnitude than the two absorption rates, the latter can dominate the change in Y_e despite being smaller in magnitude than the former.

Figure 8 shows the average change in Y_e for tracer particles as a function of disk mass in the baseline sequence with $M_{\text{bh}} = 8M_\odot$, along with the breakdown of this change between emission and absorption of electron neutrinos/antineutrinos. At low disk masses, emission processes dominate the change in Y_e , with decreasing relative importance with increasing disk mass. Emission processes act toward driving Y_e to its local equilibrium value set by the entropy, and this equilibrium is lower at higher disk masses given the lower entropy (Figure 7). At the highest disk mass (model b08d20), this change in Y_e due to emission is even negative.

Absorption, on the other hand, is set by the ambient flux of incident neutrinos and the mass fractions of neutrons and protons. At higher disk masses, neutrino/antineutrino luminosities are higher and stay high for a longer time (Figure 3) thus increasing the ambient neutrino flux and the thus the magnitude of absorption terms. The asymmetry in the neutron-proton mass fraction then results in different absorption efficiencies and a net change in Y_e which always acts in the direction of increasing it (because the reaction in eqn. 12 occurs more frequently). Figure 8 shows that at high disk masses, absorption dominates the evolution of Y_e in the high-compactness models shown. Table 3 shows that this trend is also present in models with the lowest compactness (b03d01-b03d30), with an even stronger effect of absorption on Y_e than in the high compactness sequence.

Models with lower initial $Y_e = \{0.10, 0.15\}$ eject a higher proportion of lanthanides and actinides, as expected, although the change is at a $\lesssim 10\%$ level by mass relative to our baseline parameters (Figure 9). While the Y_e distributions extend to slightly lower electron fractions than the default models, the bulk of the outflow has $Y_e > 0.2$ in all cases. Table 3 shows that these changes are driven

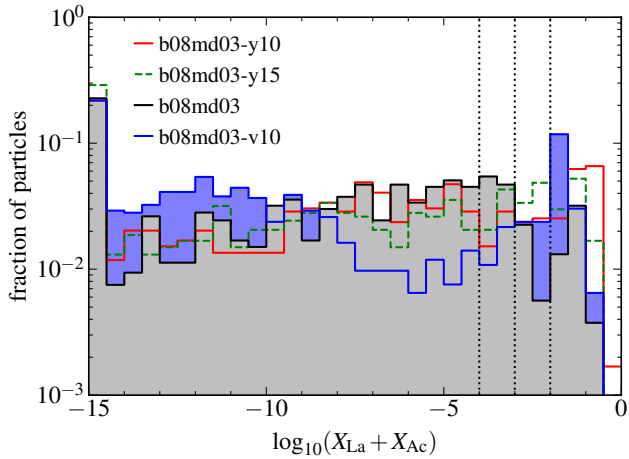


Figure 9. Distribution of lanthanide and actinide mass fractions at 1 day, for nuclear-network-processed particles from models b08d03 (baseline), b08d03-y10 and b08d03-y15 (varying initial Y_e), and b08d03-v10 (high viscosity), as labeled. The bin size is the same as in the top panel of Figure 6. The lowest bin contains all the particles with $X_{La} + X_{Ac} < 10^{-14.5}$.

primarily by neutrino emission processes, which adjust to provide the required change in Y_e toward equilibrium.

Models with higher viscosity have a similar average Y_e than their low-viscosity counterparts, but a significantly higher fraction of material rich in lanthanide and actinides. The electron fraction distribution of model b08d03-v10 has a tail to low Y_e that extends well below the lower limit of the distribution of model b08d01. Figure 7 shows that the material with the lowest Y_e is ejected at the earliest times in the high-viscosity model, in line with the general expectation that the faster the evolution of a disk, the stronger the sensitivity of the outflow composition to initial conditions (this is consistent with the results of GRMHD simulations, which show even stronger memory of initial conditions given their faster evolution; Fernández et al. 2019).

3.3 Implications for EM counterpart searches

The key question we are interested in is how does the disk outflow contribute to a kilonova transient. The answer depends on the amount of mass ejected and its velocity, its composition, as well as how efficiently does the radioactive heating thermalize (e.g., Metzger 2019).

The mass ejected, and the composition to a lesser extent, determines how much radioactive power is available for a kilonova. Figure 10 shows the total radioactive heating luminosity at 1 day as a function of compactness parameter C_d and initial disk mass. For fixed compactness, the total radioactive heating is proportional to the ejected mass, since the average radioactive heating per unit mass is close to $2 \times 10^{10} \text{ erg g}^{-1} \text{ s}^{-1}$ for most models, given their similar composition. The dependence of ejected fraction on compactness results in an additional variation of a factor ~ 5 between the least and most compact models, for fixed disk mass.

The raw radioactive heating at 1 day ranges from $2 \times 10^{40} \text{ erg s}^{-1}$ for the lightest and most compact disk (b08d01) to $1.5 \times 10^{42} \text{ erg s}^{-1}$ for the heaviest disk in the least compact configuration (b03d30). Thermalization efficiency can result in a decrease in these values by a factor ~ 2 (Barnes et al. 2016; Waxman et al. 2019; Kasen & Barnes 2019; Hotokezaka & Nakar 2020), while

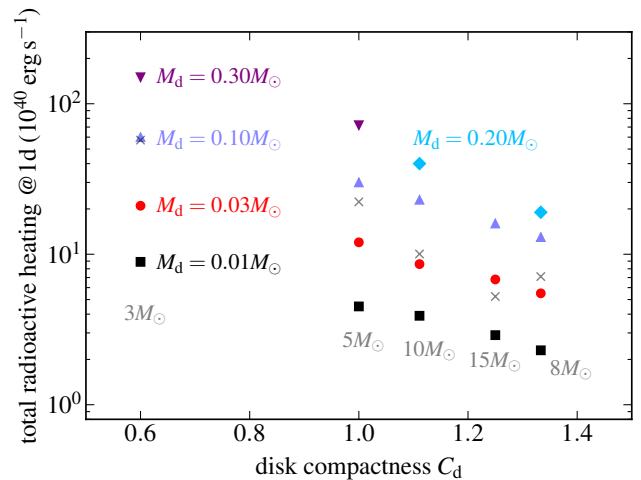


Figure 10. Total radioactive heating luminosity at 1 day as a function of disk compactness (eq. 3), for various disk masses, as labeled. The BH mass is shown in gray under each symbol column. The crosses denote the heating rates interpolated to the median disk masses from Figure 1. The total radioactive heating rate is an upper limit to the bolometric luminosity of the kilonova, being subject to thermalization efficiency and radiative transfer effects.

radiative transfer effects (dependent on the opacity and thus on composition) set whether this power can readily escape the ejecta or is trapped until later times. Table 2 shows that the radioactive power at 1 week is about 10 times smaller than that at 1 day for most models.

If we take the median disk masses from Figure 1 as representative values for each BH mass and interpolate the ejected masses from Table 2, we obtain disk outflow masses $\{2.00, 0.70, 0.22, 0.25, 0.14\} \times 10^{-2} M_\odot$ for BH masses $\{3, 5, 8, 10, 15\} M_\odot$, respectively. These values are subject to enhancement by a factor $\lesssim 2$ if GRMHD effects were to be included (Fernández et al. 2019; Christie et al. 2019).

In the case of GW190425, for which our lowest BH mass model would be applicable, the median disk outflow mass would be similar to the total ejecta from GW170817 within a factor of two, and hence it would have been detected with good sky coverage (Kyutoku et al. 2020). A BH-NS merger with a low-mass BH and high-mass NS is most efficient at tidally disrupting the NS and most inefficient at producing dynamical ejecta, with most mass ejection coming from the disk (Foucart et al. 2019). In contrast, two massive NS that collapse promptly to a BH are the least efficient configuration for ejecting mass and forming a disk (e.g., Radice et al. 2018, but see Kiuchi et al. 2019; Bernuzzi et al. 2020 for the case of an asymmetric mass ratio NS-NS merger generating a more massive BH accretion disk than a symmetric binary).

Regarding the BH-NS merger candidate S190814bv, which had a much smaller localization area and deeper EM coverage relative to other candidates, constraints on the total mass ejection are in the range $0.02 - 0.1 M_\odot$ depending on viewing angle, composition, and distance. (e.g., Andreoni et al. 2020; Kawaguchi et al. 2020b; Vieira et al. 2020). Our results indicate that, with the exception of a very low-mass BH and/or very high disk masses, most BH-NS merger systems would not have generated sufficient disk outflow for a detectable kilonova.

An additional factor influencing the kilonova appearance is the

relative masses of the disk and the dynamical ejecta. In a BH-NS merger, the dynamical ejecta is produced along the equatorial plane, and it blocks only part of the viewing angles. It is expected to be very rich in lanthanides and thus have a high opacity that blocks the light from the disk toward most equatorial directions. The results of [Fernández et al. \(2015b\)](#) and [Fernández et al. \(2017\)](#) – who studied the combined long-term evolution of these two components mapped from dynamical merger simulations – show that the bulk of fallback accretion mixes in with the disk before weak freezout occurs and the disk outflow is launched. The net outflow has a very similar composition as the dynamical ejecta and disk when evolved separately, but with an added component that has intermediate electron fraction values. The expected kilonova color has an important dependence on viewing angle, as the bluer disk emission would only be detectable from directions not obscured by the dynamical ejecta (see, e.g., [Bulla et al. 2019](#); [Darbha & Kasen 2020](#); [Kawaguchi et al. 2020a](#); [Korobkin et al. 2020](#) for more recent work on viewing angle dependencies of different ejecta configurations).

In hydrodynamic simulations of BH accretion disks, the spatial dependence of the composition is quite generic, with the highest Y_e material being ejected first along intermediate latitudes, and then wrapping around the outermost edge of the disk outflow ([Fernández et al. 2015a](#)). This configuration would guarantee the existence of a blue spike at early times (albeit a faint one) if the merger remnant is viewable from polar latitudes. All of our models are such that at least 50% of the disk outflow is lanthanide-poor, and in some cases this fraction can reach even 100% (Table 2). GRMHD models show, however, that magnetic fields begin to eject matter much earlier than weak freezout, thus adding material that has not been sufficiently processed by weak interactions from the initial post-merger composition (e.g., [Siegel & Metzger 2017](#); [Fernández et al. 2019](#); [Miller et al. 2019](#); [Christie et al. 2019](#)). This will likely increase the lanthanide-rich fraction at the leading edge of the disk outflow and thus modify the color of the disk-contributed kilonova.

4 SUMMARY AND DISCUSSION

We have performed axisymmetric hydrodynamic simulations of the viscous evolution of accretion disks formed in BH-NS mergers. Our models include the effects of neutrino emission and absorption on the outflow composition, and the results are post-processed with a nuclear reaction network for a more precise diagnostic of the nucleosynthesis yield. These hydrodynamic models provide a lower-limit to the amount of mass in the disk outflow relative to three-dimensional GRMHD models, and hence provide a lower-limit to the contribution of disk outflows to the kilonova transient. Our simulations cover, for the first time, a large fraction of the plausible parameter space of BH and disk masses expected from these mergers (Figure 1). Our main results are the following:

1. – The fraction of the initial disk mass ejected as an unbound outflow has an approximately inverse linear scaling with the initial compactness of the disk, and can vary by a factor of ~ 4 (Figure 2 and Table 2). While this dependence on compactness was implicit in previous work, this is the first time that it is systematically probed over a wide parameter space.

The origin of this dependence can be traced back to the earlier onset of accretion in more compact disks, as they are located closer to the ISCO. Compared to lower compactness disks, a higher fraction of the initial mass is accreted by the time weak interactions freeze

out and the outflow is launched (Figure 3).

2. – At constant compactness, the fraction of the disk mass ejected decreases for higher disk masses. This effect is related to the longer time to reach weak freezout in more massive disks, which delays the onset of mass ejection to a time when more mass has been accreted to the BH (Figure 3). The dependence on initial disk mass is weaker for higher compactness systems (Figure 2 and Table 2). The initial density and entropy of the disk are the key variables regulating this mass dependency of the ejection efficiency (§3.1).

3. – The disk outflow is more lanthanide/actinide-poor for higher disk masses (Figure 6), at constant compactness (this trend has also been found in previous studies). This effect can be traced back to neutrino absorption becoming more important relative to emission in increasing Y_e for more massive disks (Figure 8 and Table 3). Stronger absorption counteracts the action of neutrino emission in lowering Y_e given the lower entropy of the outflow from more massive disks (Figure 7).

While our disk outflows are 50 – 100% lanthanide-poor by mass, magnetically driven contributions – not included here – can add a significant amount of lanthanide-rich matter, hence the net composition of disk outflows requires simulations with more complete physics for reliable predictions.

4. – The ejected fraction and final composition are sensitive to the viscosity parameter of the disk, as known from previous work, with more mass ejected, at higher velocities, and with a higher lanthanide-rich fraction for higher viscosity parameter (Table 2). The most neutron-rich material is produced at the earliest times in the simulation (Figure 7) and is thus related to the shorter evolution time of these disks.

5. – In most cases, the initial Y_e of the disk has a negligible effect on the amount of mass ejected, with the exception of massive disks in low-compactness systems, where the effect modifies the ejection efficiency by a few percent of the disk mass (similar to numerical resolution). Hence, the ejected fraction is mostly robust to variations in the initial composition (Table 2). The final composition does depend on the initial conditions, with corrections of the order of 10% to the fraction of the outflow mass that is lanthanide-rich (Figure 9)

6. – The range of ejecta masses from the disk outflow can result in a range of two orders of magnitude in raw radioactive luminosity over the BH-NS parameter space probed (Figure 10). Except for very low-mass BHs and/or very high disk masses, most BH-NS mergers should generate disk outflows that are below constraints for the total ejecta mass from the BH-NS merger candidate S190814bv (§3.3).

Our results are consistent with previous hydrodynamic models of BH accretion disks. Model t-a80-hr from [Fernández et al. \(2015a\)](#) is equivalent to our model b03d01 but evolved until 3,000 orbits. By that time, the total and unbound (positive energy) mass ejected in their model are 19% and 12%, respectively, while here we obtain 21% and 14%, respectively. The $\sim 10\%$ difference can be attributed to the lower ambient and floor of density used here, and on improvements in the neutrino implementation as reported in [Lippuner et al. \(2017\)](#). Similarly, model Fdisk of [Fernández et al. \(2017\)](#) falls in between models b08d03 and b08d10 in terms of

compactness, but has a slightly higher BH spin (0.86). The higher ejected fraction in their model (8%) can be partially accounted for by the higher value of the BH spin, and also by a more extended initial density distribution with radius in the torus mapped from the merger simulation (covering a wider range in compactness)

We have made specific choices for the disk entropy (§2.1), which can have implications for the sensitivity of the ejected fraction to initial disk mass. Similarly, the choice of viscosity parameter is on the low end of values that bracket the amount of angular momentum transport seen in GRMHD simulations of equivalent accretion disks (Fernández et al. 2019). More realistic values for these two parameters must come from direct mapping of the outcome of GRMHD simulations of BH-NS mergers that include neutrino transport, where the magnetic field geometry and strength replaces the viscosity parameter. This would also inform the initial Y_e distribution which, while not crucial for determining the amount of mass ejected, has implications for the outflow composition at the level of detail needed for accurate predictions of kilonovae and nucleosynthesis yields. Such compact object merger simulations are only beginning to be carried out at the time of this writing (e.g., Most et al. 2019).

Our results suggest that GRMHD simulations carried out with no neutrino absorption (e.g., Siegel & Metzger 2018; Fernández et al. 2019; Christie et al. 2019) can give reasonable Y_e distributions only for very low mass disks $< 0.01 M_\odot$, for which the absorption contribution to Y_e is subdominant. For the configuration studied by Siegel & Metzger (2018), Fernández et al. (2019), and Christie et al. (2019) ($M_{\text{bh}} = 3 M_\odot$ and $M_{\text{d}} = 0.03 M_\odot$), we find that absorption is already more important than emission in setting the Y_e distribution (Table 3), in line with the results of Miller et al. (2019) who showed a significant increase in the Y_e of the outflow when including neutrino absorption.

Further GRMHD studies of BH accretion disks over a wide region of parameter space are needed to determine whether the ejected fraction has the same dependence on compactness as in pure hydrodynamic models, and whether the fraction of the outflow that is lanthanide-rich is significantly larger than what we find here. Both of these questions are crucial to improve predictions of EM counterparts to BH-NS and NS-NS sources, and require (1) models evolved for long timescales, (2) realistic initial field strengths, geometries, entropies, and electron fractions, and (3) inclusion of neutrino absorption. Such simulations remain challenging given current algorithms and computational resources.

ACKNOWLEDGEMENTS

RF acknowledges support from the National Sciences and Engineering Research Council (NSERC) of Canada through Discovery Grant RGPIN-2017-04286, and from the Faculty of Science at the University of Alberta. FF gratefully acknowledges support from the U.S. National Science Foundation (NSF) through grant PHY-1806278, from the National Aeronautics and Space Administration (NASA) through grant 80NSSC18K0565, and from the U.S. Department of Energy CAREER grant DE-SC0020435. This work was supported by the U.S. Department of Energy through the Los Alamos National Laboratory. Los Alamos National Laboratory is operated by Triad National Security, LLC, for the National Nuclear Security Administration of U.S. Department of Energy (Contract No. 89233218CNA000001). This work was assigned report number LA-UR-20-23877. The software used in this work was in part developed by the U.S. Department of Energy NNSA-ASC OASCR Flash Cen-

ter at the University of Chicago. This research was enabled in part by support provided by WestGrid (www.westgrid.ca), the Shared Hierarchical Academic Research Computing Network (SHARCNET, www.sharcnet.ca), Calcul Québec (calculquebec.ca), and Compute Canada (www.computecanada.ca). Computations were performed on *Graham*, *Cedar*, and *Béluga*. This research also used storage resources of the U.S. National Energy Research Scientific Computing Center (NERSC), which is supported by the Office of Science of the U.S. Department of Energy under Contract No. DE-AC02-05CH11231 (repository m2058). Graphics were developed with `matplotlib` (Hunter 2007).

REFERENCES

- Abbott B. P., et al., 2017, *ApJ*, **848**, L12
 Abbott B. P., et al., 2019, *Physical Review X*, **9**, 031040
 Abbott B. P., et al., 2020, *ApJ*, **892**, L3
 Ackley K., et al., 2020, preprint, [arXiv:2002.01950](https://arxiv.org/abs/2002.01950)
 Andreoni I., et al., 2020, *ApJ*, **890**, L13
 Artemova I. V., Bjoernsson G., Novikov I. D., 1996, *ApJ*, **461**, 565
 Barbieri C., Salafia O. S., Colpi M., Ghirlanda G., Perego A., Colombo A., 2019, *ApJ*, **887**, L35
 Barnes J., Kasen D., 2013, *ApJ*, **775**, 18
 Barnes J., Kasen D., Wu M.-R., Martínez-Pinedo G., 2016, *ApJ*, **829**, 110
 Beloborodov A. M., 2003, *ApJ*, **588**, 931
 Bernuzzi S., et al., 2020, preprint, [arXiv:2003.06015](https://arxiv.org/abs/2003.06015)
 Bethe H. A., Applegate J. H., Brown G. E., 1980, *ApJ*, **241**, 343
 Bludman S. A., van Riper K. A., 1978, *ApJ*, **224**, 631
 Bulla M., et al., 2019, *Nature Astronomy*, **3**, 99
 Chen W.-X., Beloborodov A. M., 2007, *ApJ*, **657**, 383
 Christie I. M., Lalakos A., Tchekhovskoy A., Fernández R., Foucart F., Quataert E., Kasen D., 2019, *MNRAS*, **490**, 4811
 Coughlin M. W., et al., 2020, *MNRAS*, **492**, 863
 Cyburt R. H., et al., 2010, *ApJS*, **189**, 240
 Darbha S., Kasen D., 2020, preprint, [arXiv:2002.00299](https://arxiv.org/abs/2002.00299)
 Di Matteo T., Perna R., Narayan R., 2002, *ApJ*, **579**, 706
 Dubey A., Antypas K., Ganapathy M. K., Reid L. B., Riley K., Sheeler D., Siegel A., Weide K., 2009, *J. Par. Comp.*, **35**, 512
 Eichler M., Sayar W., Arcones A., Rauscher T., 2019, *ApJ*, **879**, 47
 Fahlman S., Fernández R., 2018, *ApJ*, **869**, L3
 Fernández R., Metzger B. D., 2013, *MNRAS*, **435**, 502
 Fernández R., Metzger B. D., 2016, *ARNPS*, **66**, 23
 Fernández R., Kasen D., Metzger B. D., Quataert E., 2015a, *MNRAS*, **446**, 750
 Fernández R., Quataert E., Schwab J., Kasen D., Rosswog S., 2015b, *MNRAS*, **449**, 390
 Fernández R., Foucart F., Kasen D., Lippuner J., Desai D., Roberts L. F., 2017, *CQG*, **34**, 154001
 Fernández R., Tchekhovskoy A., Quataert E., Foucart F., Kasen D., 2019, *MNRAS*, **482**, 3373
 Foley R. J., Coulter D. A., Kilpatrick C. D., Piro A. L., Ramirez-Ruiz E., Schwab J., 2020, *MNRAS*, **494**, 190
 Fontes C. J., Fryer C. L., Hungerford A. L., Hakel P., Colgan J., Kilcrease D. P., Sherrill M. E., 2015, *High Energy Density Physics*, **16**, 53
 Foucart F., Hinderer T., Nisanke S., 2018, *Phys. Rev. D*, **98**, 081501
 Foucart F., Duez M. D., Kidder L. E., Nisanke S. M., Pfeiffer H. P., Scheel M. A., 2019, *Phys. Rev. D*, **99**, 103025
 Frankel S., Metropolis N., 1947, *Physical Review*, **72**, 914
 Fryxell B., et al., 2000, *ApJS*, **131**, 273
 Fujibayashi S., Shibata M., Wanajo S., Kiuchi K., Kyutoku K., Sekiguchi Y., 2020, *PRD*, **101**, 083029
 Fuller G. M., Fowler W. A., Newman M. J., 1982, *ApJS*, **48**, 279
 Goriely S., 1999, *A&A*, **342**, 881
 Hinderer T., et al., 2019, *Phys. Rev. D*, **100**, 063021
 Holmbeck E. M., Sprouse T. M., Mumpower M. R., Vassh N., Surman R., Beers T. C., Kawano T., 2019, *ApJ*, **870**, 23

- Hossein Nouri F., et al., 2018, *Phys. Rev. D*, **97**, 083014
- Hotokezaka K., Nakar E., 2020, *ApJ*, **891**, 152
- Hunter J. D., 2007, *Computing In Science & Engineering*, **9**, 90
- Just O., Bauswein A., Pulpillo R. A., Goriely S., Janka H.-T., 2015, *MNRAS*, **448**, 541
- Kasen D., Barnes J., 2019, *ApJ*, **876**, 128
- Kasen D., Badnell N. R., Barnes J., 2013, *ApJ*, **774**, 25
- Kasen D., Fernández R., Metzger B. D., 2015, *MNRAS*, **450**, 1777
- Kawaguchi K., Kyutoku K., Shibata M., Tanaka M., 2016, *ApJ*, **825**, 52
- Kawaguchi K., Shibata M., Tanaka M., 2020a, *ApJ*, **889**, 171
- Kawaguchi K., Shibata M., Tanaka M., 2020b, *ApJ*, **893**, 153
- Kiuchi K., Kyutoku K., Shibata M., Taniguchi K., 2019, *ApJ*, **876**, L31
- Korobkin O., et al., 2020, preprint, arXiv:2004.00102
- Krüger C. J., Foucart F., 2020, preprint, arXiv:2002.07728
- Kyutoku K., Fujibayashi S., Hayashi K., Kawaguchi K., Kiuchi K., Shibata M., Tanaka M., 2020, *ApJ*, **890**, L4
- LIGO Scientific Collaboration Virgo Collaboration 2019, GCN Circular, 25324
- LIGO Scientific Collaboration Virgo Collaboration 2020, preprint, arXiv:2004.08342
- Langanke K., Martínez-Pinedo G., 2000, *Nuclear Phys. A*, **673**, 481
- Lee W. H., Ramirez-Ruiz E., López-Cámara D., 2009, *ApJ*, **699**, L93
- Lippuner J., Roberts L. F., 2015, *ApJ*, **815**, 82
- Lippuner J., Roberts L. F., 2017, *ApJS*, **233**, 18
- Lippuner J., Fernández R., Roberts L. F., Foucart F., Kasen D., Metzger B. D., Ott C. D., 2017, *MNRAS*, **472**, 904
- Mamdouh A., Pearson J. M., Rayet M., Tondeur F., 2001, *Nuclear Phys. A*, **679**, 337
- Metzger B. D., 2019, *Living Reviews in Relativity*, **23**, 1
- Metzger B. D., Fernández R., 2014, *MNRAS*, **441**, 3444
- Metzger B. D., Piro A. L., Quataert E., 2009, *MNRAS*, **396**, 304
- Miller J. M., et al., 2019, *Phys. Rev. D*, **100**, 023008
- Möller P., Sierk A. J., Ichikawa T., Sagawa H., 2016, *Atomic Data and Nuclear Data Tables*, **109**, 1
- Most E. R., Papenfort L. J., Tsokaros A., Rezzolla L., 2019, *ApJ*, **884**, 40
- Oda T., Hino M., Muto K., Takahara M., Sato K., 1994, *Atomic Data and Nuclear Data Tables*, **56**, 231
- Pannarale F., 2014, *Phys. Rev. D*, **89**, 044045
- Panov I. V., Korneev I. Y., Rauscher T., Martínez-Pinedo G., Kelić-Heil A., Zinner N. T., Thielemann F. K., 2010, *A&A*, **513**, A61
- Popham R., Woosley S. E., Fryer C., 1999, *ApJ*, **518**, 356
- Radice D., Perego A., Hotokezaka K., Fromm S. A., Bernuzzi S., Roberts L. F., 2018, *ApJ*, **869**, 130
- Roberts L. F., et al., 2017, *MNRAS*, **464**, 3907
- Shakura N. I., Sunyaev R. A., 1973, *A&A*, **24**, 337
- Shibata M., Hotokezaka K., 2019, *Annual Review of Nuclear and Particle Science*, **69**, 41
- Siegel D. M., Metzger B. D., 2017, *Physical Review Letters*, **119**, 231102
- Siegel D. M., Metzger B. D., 2018, *ApJ*, **858**, 52
- Stone J. M., Pringle J. E., Begelman M. C., 1999, *MNRAS*, **310**, 1002
- Tanaka M., Hotokezaka K., 2013, *ApJ*, **775**, 113
- Tanaka M., Kato D., Gaigalas G., Kawaguchi K., 2019, preprint, arXiv:1906.08914
- Timmes F. X., Swesty F. D., 2000, *ApJS*, **126**, 501
- Vieira N., et al., 2020, preprint, arXiv:2003.09437
- Wahl A. C., 2002, Technical Report LA-13928. Systematics of fission-product yields. Los Alamos National Laboratory, Los Alamos, NM
- Waxman E., Ofek E. O., Kushnir D., 2019, *ApJ*, **878**, 93
- Wu M.-R., Fernández R., Martínez-Pinedo G., Metzger B. D., 2016, *MNRAS*, **463**, 2323

This paper has been typeset from a $\text{\TeX}/\text{\LaTeX}$ file prepared by the author.